Tellus (2002), 54A, 512–528
Printed in UK. *All rights reserved*

Copyright © Blackwell Munksgaard, 2002
TELLUS
ISSN 0280-6495

Simulating the Greenland atmospheric boundary layer

Part I: Model description and validation

By BRUCE DENBY*, WOUTER GREUELL and JOHANNES OERLEMANS, *Institute for Marine and Atmospheric Research, Utrecht University, Princetonplein 5, 3584 CC Utrecht, The Netherlands*

(Manuscript received 7 December 2001; in final form 22 April 2002)

ABSTRACT

A three-dimensional dynamic downscaling model of the Greenland atmospheric boundary layer, with a horizontal resolution of 20 km, is descibed and applied to the Greenland ice sheet for the 1998 ablation season. The model uses ECMWF analysis data fields of synoptic pressure, free atmospheric temperature, cloud cover, humidity and sea surface temperature to force the model. The model calculates the perturbation component of the temperature and pressure field to describe the atmospheric boundary layer dynamics. The aim of this study, the first of two papers, is to investigate the role of the turbulent heat fluxes in the surface energy balance of the ice sheet and their response to changes in atmospheric temperature. In this first paper, results from the simulation are compared with observations from six automatic weather stations situated on the ice sheet, three in the ablation zone and three in the accumulation zone. The comparison shows that the boundary layer model can reproduce the near-surface meteorological variables of wind, temperature and specific humidity quite well and improve significantly on 2 m values taken directly from the ECMWF analysis. The increased spatial resolution of the model is essential in order to model accurately katabatically forced winds near the margin of the ice sheet. The calculated and observed melts at two sites in the ablation zone are also compared. At one site close to the margin, which is situated in a well drained ice region, the comparison with observations is very good, within 1%. At a higher site, where subsurface processes not included in the model are important for the total ablation, the calculated melt is 35% larger than the observed ablation.

1. Introduction

The surface mass balance of ice sheets and glaciers is determined by accumulation and ablation. Accumulation is the rate at which mass is added to the surface, through solid precipitation, and ablation is the rate at which it is lost, chiefly through melt and sublimation. On the Greenland ice sheet it is currently estimated that half of all mass loss is via calving at the ice–sea interface, the other half is the result of ablation via surface melt (Reeh et al., 1999). In order to quantify the mass balance of the Greenland ice sheet it is necessary to determine these ablation rates and their sensitivity to climatic variations.

The ablation rate is directly determined by the surface energy balance (SEB), which consists of short- and longwave radiation fluxes as well as sensible and latent turbulent heat fluxes. The most important component of the SEB during summer is the absorbed shortwave radiation. This is dependent chiefly on surface albedo and secondly on cloud type and distribution, as well as atmospheric temperature and humidity. However, changes in atmospheric conditions, such as temperature and circulation patterns, have a more important influence on the three other components of the SEB. Atmospheric temperature, humidity and wind speed are determinant for the turbulent heat fluxes at the surface. Likewise atmospheric temperature, humidity and cloud cover are important for determining the incoming longwave radiation.

*Corresponding author.
e-mail: bd236@cam.ac.uk
Present address: Scott Polar Research Institute, University of Cambridge Lensfield Road, Cambridge CB2 1ER, UK.

Currently the ablation components of mass balance models vary in their sophistication, ranging from simple degree day models, e.g. Reeh (1991), to complete energy balance models driven by observed wind, temperature and radiation fluxes, e.g Greuell and Konzelmann (1994). Degree day models are highly parameterised ablation models that relate near-surface temperatures to ablation rates via a degree day factor. Energy balance models, on the other hand, represent as completely as possible the physics behind ablation and are thus more appropriate for extrapolation into unknown climate scenarios than degree day models, which are empirically based on present day observations. Even so, energy balance models are often based on simplified assumptions. In particular, and the main focus of this study, the turbulent sensible and latent heat fluxes are often prescribed as a linear function of atmospheric temperature at some predefined height, usually 2 m (van de Wal, 1994; Zuo and Oerlemans, 1996). This simplification excludes variations in wind speed even though turbulent exchange is directly dependent upon it. Climatic changes in free atmospheric temperatures are also often assumed to be equivalent to changes in 2 m temperatures (van de Wal, 1994). Above a melting ice surface this is not the case, since the 2 m temperature is strongly influenced by the surface temperature, which remains constant during melt, and so temperature changes at 2 m will be less than those in the free atmosphere.

The state of the free atmosphere is translated down to the surface through the atmospheric boundary layer (ABL). Conditions within the ABL are the result of boundary layer dynamics, such as katabatic flows on sloping surfaces, and a mixture of both surface conditions, e.g. surface roughness and temperature, as well as free atmospheric conditions. Determination of the turbulent flux and incoming longwave radiation at the surface will require some physical description of the ABL itself.

The Greenland atmospheric boundary layer model (GABLM) is developed to improve estimates of the surface energy flux, particularly the turbulent heat fluxes, on the Greenland ice sheet. The model uses prescribed boundary and initial conditions such as synoptic pressure gradients, temperature and humidity fields, cloud cover and height, and various surface parameters in order to force the ABL above the Greenland ice sheet. The atmospheric input fields are taken from ECMWF analysis data. The aim is to downscale these fields dynamically in order to translate them directly into surface energy fluxes which can be used in mass balance modelling.

Since ablation occurs in a narrow region near the ice margin, on average 30 km wide and no more than 100 km wide at its greatest extent, typical atmospheric models cannot resolve this region to a sufficient degree of accuracy. As such, any atmospheric model used to simulate the surface energy fluxes would require a resolution significantly greater than 100 km. ECMWF analysis data, for instance, have a resolution of T213, approximately 70 km, and are not capable of resolving the ablation zone of Greenland. The model developed here has a horizontal resolution of 20 km which allows it to resolve the ablation zone to a reasonable degree.

In this and a concurrent paper (Denby et al., 2002) use is made of the GABLM to determine the SEB and near-surface meteorological variables on the Greenland ice sheet. Simulations are carried out for the 1998 ablation season, for which observational data from six automatic weather stations on the ice sheet are available. In this study the GABLM is described and verified with these observations. In the concurrent article the energy balance and its climate sensitivity are discussed. The emphasis of both these papers lies with the determination of the turbulent heat flux components, their contribution to melt and their climatic sensitivity.

2. Model description

The GABLM is a three-dimensional (3-D) hydrostatic ABL model based on the basic dynamic and thermodynamic equations. It incorporates a second-order closure turbulence scheme, a longwave emissivity scheme to determine longwave radiation in the ABL and a subsurface temperature diffusion model. Surface parameters and cloud cover are prescribed, and the model is forced at the top and lateral boundaries by ECMWF analysis data.

2.1. *Dynamics*

The boundary layer model is based on the basic conservation laws that can be found in many texts, e.g. Pielke (1984). The equations describing conservation of momentum are written in their scaled pressure form as follows:

$$\frac{\mathrm{D}U_i}{\mathrm{D}t} = -\frac{\partial \overline{u_i u_j}}{\partial x_j} - \bar{\Theta}\frac{\partial \bar{\Pi}}{\partial x_i} - g_i - f\epsilon_{i3k}U_k \tag{1}$$

The velocity components in the above equation are separated into their turbulent (lower-case) and mean (upper-case) values by way of Reynolds decomposition. This equation can be simplified and transformed for use in mesoscale models over inclined terrain. The total Exner function $\bar{\Pi}$ and potential temperature $\bar{\Theta}$ are split into their synoptic (Π_o, Θ_o) and mesoscale, or perturbation, components (Π, Θ) and the hydrostatic assumption for the synoptic components, i.e. $\Theta_o(\partial\Pi_o/\partial z) = -g$, where g is the acceleration due to gravity, is also applied.

It is then useful to transform the coordinate system to a terrain-influenced system where the lowest model level follows the terrain surface and returns to a horizontal surface at the top of the model domain. This is done by way of the transformation matrix as described in Anderson et al. (1984), Gal-Chen and Somerville (1975) or Pielke (1984). The simplest and most suitable coordinate transformation for the present model is that of equidistant orthogonal horizontal coordinates (x, y) and stretched terrain-influenced vertical coordinates. Vertical stretching is logarithmic, so that the grid spacing is smallest near the surface, where gradients of meteorological variables are largest. The model grid is then transformed to follow the surface terrain. The resulting transformation metrics which transform the real Cartesian coordinate system (x_i) to the equidistant computational coordinate system $(\tilde{x}_i)$ can be written as follows:

$$J^{ij} = \frac{\partial x_i}{\partial \tilde{x}_j} = \begin{bmatrix} 1 & 0 & 0 \\ 0 & 1 & 0 \\ \dfrac{\partial z}{\partial \tilde{x}} & \dfrac{\partial z}{\partial \tilde{y}} & \dfrac{\partial z}{\partial \tilde{z}} \end{bmatrix} \tag{2}$$

where $U_i = J^{ij}\tilde{U}_j$ and $\partial/\partial x_i = J_{ij}(\partial/\partial \tilde{x}_j)$. The two transformation metrics are related to each other by their inverse, i.e. $J_{ij} = J^{ij^{-1}}$.

With the grid transformation made here, only three terms in the transformation metric need be determined, i.e. J_{zz}, which defines the vertical stretching of the grid, and J_{zx} and J_{zy}, which define the slope of the grid in the x and y directions. At the surface these last two terms are equivalent to the surface slope. Application of these metrics and the simplifications described above give the following two equations for the horizontal wind components (U, V), where the tilde is dropped from the horizontal components since these are unaltered by the coordinate transformation.

$$\frac{\mathrm{d}U}{\mathrm{d}t} = -J_{zz}\frac{\partial\overline{uw}}{\partial\tilde{z}} - \Theta_o\frac{\partial\Pi}{\partial x} + J_{zx}\frac{g}{\Theta_o}\Theta + f(V - V_g) \tag{3}$$

$$\frac{\mathrm{d}V}{\mathrm{d}t} = \underbrace{-J_{zz}\frac{\partial\overline{vw}}{\partial\tilde{z}}}_{\text{flux divergence}} \underbrace{- \Theta_o\frac{\partial\Pi}{\partial y}}_{\text{pressure gradient}} \underbrace{+ J_{zy}\frac{g}{\Theta_o}\Theta}_{\text{katabatic}} \underbrace{- f(U - U_g)}_{\text{Coriolis}} \tag{4}$$

where

$$\frac{\mathrm{d}}{\mathrm{d}t} = \frac{\partial}{\partial t} \underbrace{+ U\frac{\partial}{\partial x} + V\frac{\partial}{\partial y}}_{\text{horizontal advection}} \underbrace{+ \tilde{W}\frac{\partial}{\partial\tilde{z}}}_{\text{vertical entrainment}} \tag{5}$$

and where the geostrophic wind fields are given by

$$U_g = -\frac{\Theta_o}{f}\frac{\partial\Pi_o}{\partial y} \quad \text{and} \quad V_g = \frac{\Theta_o}{f}\frac{\partial\Pi_o}{\partial x} \tag{6}$$

and f is the Coriolis parameter. In the above equations the flux divergence terms are simplified by including only the vertical gradient terms, since horizontal gradients are generally much smaller.

The transformed vertical component of motion $\tilde{W}$ is deduced from the continuity equation and is assumed to be in hydrostatic equilibrium, so that the scaled pressure perturbation can be determined by integrating

$$J_{zz}\frac{\partial\Pi}{\partial\tilde{z}} = \frac{g}{\Theta_o^2}\Theta \tag{7}$$

with the assumption that Π at the top of the model domain is equal to zero. The hydrostatic assumption applied in this fashion on terrain-influenced coordinates is applicable only for slopes $<5°$ (Pielke, 1984).

Conservation of entropy, which leads to the prognostic equation for potential temperature, is written as follows:

$$\frac{\mathrm{D}\bar{\Theta}}{\mathrm{D}t} = -\frac{\partial\overline{u_j\theta}}{\partial x_j} - \frac{1}{c_p\rho}\frac{\partial R_j}{\partial x_j} \tag{8}$$

where $\overline{u_j\theta}$ is the turbulent temperature flux and R_j is the net radiation flux, both oriented in the j direction. As previously mentioned, the total potential temperature $\bar{\Theta}$ is split into a synoptic, or ambient, component $\Theta_o(x, y, z)$ and a perturbation component $\Theta(x, y, z)$. By assuming vertical gradients to be much larger than horizontal gradients, the transformed equations for potential temperature perturbation (Θ) and water vapour (Q) become

$$\frac{\mathrm{d}\Theta}{\mathrm{d}t} = -J_{zz}\frac{\partial\overline{w\theta}}{\partial\tilde{z}} - \frac{J_{zz}}{c_p\rho}\frac{\partial R_z}{\partial\tilde{z}} - \frac{\mathrm{d}\Theta_o}{\mathrm{d}t} \tag{9}$$

$$\frac{\mathrm{d}Q}{\mathrm{d}t} = \underbrace{-J_{zz}\frac{\partial\overline{wq}}{\partial\tilde{z}}}_{\text{flux divergence}} \quad \text{radiation divergence} \tag{10}$$

where

$$\frac{\mathrm{d}\Theta_o}{\mathrm{d}t} = \frac{\partial\Theta_o}{\partial t} + \underbrace{U\frac{\partial\Theta_o}{\partial x} + V\frac{\partial\Theta_o}{\partial y} + \tilde{W}\frac{\partial\Theta_o}{\partial\tilde{z}}}_{\text{ambient advection}} \tag{11}$$

Since Θ_o is prescribed in the model, the time-dependent term in Eq. (11) is also prescribed. No attempt is made to include diabatic processes such as cloud formation in this model.

2.2. Turbulence scheme

The turbulence scheme is based on previous work from Denby (1999) which describes the application of a complete second-order closure model for katabatic flows. The original scheme, based on earlier work from Hanjalić and Launder (1972) and Shir (1973), involves the use of 11 turbulent prognostic equations. In Denby (1999) it was shown that one could simplify the turbulence model down to a prognostic equation for turbulent kinetic energy (E) and vertical velocity variation ($\overline{ww}$) for the type of atmospheric flow present on the Greenland ice sheet. This simplification allows the turbulent fluxes to be described in terms of generalised K-theory, where the diffusion coefficient K is diagnosed from the prognostic equations for E and $\overline{ww}$. These equations are listed in the appendix.

Monin–Obukhov theory is used at the bottom level of the model to describe the boundary conditions for the mean variables and turbulent fluxes. The surface fluxes are thus related to the stability parameter Ψ and the mean components of wind, temperature and water vapour at the lowest model level z_1 in the following way:

$$\overline{uw}_s = -\frac{\kappa^2 U(z_1)\,|\mathbf{U}(z_1)|}{(\ln(z_1/z_o) - \Psi_m)^2} \tag{12}$$

$$\overline{vw}_s = -\frac{\kappa^2 V(z_1)\,|\mathbf{U}(z_1)|}{(\ln(z_1/z_o) - \Psi_m)^2} \tag{13}$$

$$\overline{w\theta}_s = -\frac{\kappa^2(\Theta(z_1) - \Theta_s)\,|\mathbf{U}(z_1)|}{(P_r\ln(z_1/z_h) - \Psi_h)(\ln(z_1/z_o) - \Psi_m)} \tag{14}$$

$$\overline{wq}_s = -\frac{\kappa^2(Q(z_1) - Q_s)\,|\mathbf{U}(z_1)|}{(P_r\ln(z_1/z_q) - \Psi_q)\,(\ln(z_1/z_o) - \Psi_m)} \tag{15}$$

In the above equations the subscript s denotes surface values, κ is the von Karman constant (0.4) and z_o, z_h and z_q are the roughness lengths for momentum, temperature and water vapour, respectively. The stability parameters Ψ are the integrated form of the flux-profile relationships ϕ and are listed in Garratt (1992) for both stable and unstable conditions. The turbulent Prandtl number is given as $P_r = 0.92$ as is used for near-neutral conditions in Denby (1999).

2.3. Longwave radiation scheme

The incoming and outgoing longwave fluxes are calculated using the emissivity approximation from Garratt and Brost (1982) given by

$$\begin{aligned} L\downarrow(z) &= \int_z^{\infty} \sigma T(z')^4 \frac{\partial\varepsilon(z',z)}{\partial z'}\,\mathrm{d}z' \\ L\uparrow(z) &= \int_z^{0} \sigma T(z')^4 \frac{\partial\varepsilon(z',z)}{\partial z'}\,\mathrm{d}z' \\ &\quad + \varepsilon_s\sigma T_s^4[1 - \varepsilon(z, z_s)] \end{aligned} \tag{16}$$

where the Stefan–Boltzman constant $\sigma = 5.67 \times 10^{-8}$ W m^{-2} K^{-4}, T is the temperature in Kelvin and the subscript s denotes surface values. The emissivity ε is calculated for water vapour using the scheme from Welch and Zdunkowski (1976) and for CO_2 using a scheme from Rodgers (1967). Liquid water is also included at levels where clouds are specified, and the emissivity is calculated as a fraction of cloud coverage. The total emissivity ε is thus written as:

$$(1 - \varepsilon) = (1 - \varepsilon_{wv})\left(1 - \varepsilon_{CO_2}\right)(1 - n\varepsilon_{lw}) \tag{17}$$

where n is the fractional cloud cover. The net vertical radiation is calculated at any height from

$$R_z = L\uparrow(z) - L\downarrow(z)\,. \tag{18}$$

2.4. Shortwave radiation parameterisation

The incoming shortwave radiation at the surface is calculated in the following way

$$S_s = S_o\tau_{cs}\tau_{cl} \tag{19}$$

where S_o is the incoming short wave radiation at the top of the atmosphere using the formulation found in Iqbal (1983). τ_{cs} and τ_{cl} are the clear and cloudy sky attenuations, which are calculated using the parameterisations from van de Wal (1994) and Konzelmann et al. (1994) respectively. These parameterisations are based on measurements made along the K-transect, a transect of seven automatic weather stations (AWS) placed to the east of Kangerlussuaq during the Greenland Ice Margin Experiment (GIMEX) in 1991. The attenuations are given as:

$$\tau_{cs} = (0.75 + 6.8 \times 10^{-5}h + 7.1 \times 10^{-9}h^2) \times (1 - 9.0 \times 10^{-4}Z) \quad (20)$$

$$\tau_{cl} = 1 - 0.78n^2 e^{-0.00085h} \quad (21)$$

where h is the elevation in metres above sea level (a.s.l.), Z the zenith angle in degrees and n the cloud cover (0–1).

2.5. *Surface and subsurface parameters*

In the model most surface parameters are prescribed and not diagnosed from the model itself. The prescribed surface parameters are surface roughness lengths, sea surface temperature, deep soil and ice temperatures and the subsurface parameters of density, specific heat and thermal conductivity. These parameters are coupled to a parameterised surface temperature field, Eq. (22), since there is a direct physical relationship between the state of the surface and temperature. Use of this temperature field is limited to the determination of these surface parameters and to the initialisation of the model surface temperature.

2.5.1. Initial surface temperature parameterisation. A surface climatological temperature field is used to determine the spatial distribution of several of the surface and subsurface parameters and to initialise subsurface temperatures. This is based on the parameterisation from Ohmura (1987), taken from surface observations made in the period 1953–1981. This temperature field uses measurements made both on tundra and ice surfaces and is the same parameterisation used by van de Wal (1994) to drive his energy balance model of the Greenland ice sheet. The daily average surface temperature field, in °C, is described by

$$T(\phi, h, day) = T_{an} - T_{amp} \cos\left(\frac{2\pi(day - 3)}{365}\right) \quad (22)$$

where the average annual temperature is given by

$$T_{an} = 49.13 - 0.7576\phi - 0.007992h$$

Table 1. *Surface parameters for the 4 different surface types specified in the model*

Parameter	Water	Tundra	Ice	Snow
Roughness length, z_o (mm)	Eq. 23	20	20	1
Density, ρ (kg m^{-3})	1000	1600	910	200
Thermal conductivity k_s (W m^{-1} K^{-1})	∞	0.3	2.0	0.2
Specific heat c_s (J kg^{-1} K^{-1})	4186	800	2100	2100

and h is the elevation a.s.l., ϕ the latitude in degrees and *day* the Julian day. The amplitude of the annual variation is given by

$$T_{amp} = -18.35 + 0.4314\phi + 0.00172h.$$

Regions of ice and snow in the model are defined using yearly average isotherms based on this parameterisation. The ice and snow isotherms are given by $T_{ice} = -5.7\,°C$ and $T_{snow} = -19.0\,°C$, respectively. These isotherms, and their corresponding latitude-dependent heights h_{ice} and h_{snow}, are used to delineate between differing surface and subsurface parameters. Below h_{ice} parameters are given their ice value and above h_{snow} parameters are given their snow value (Table 1). These are linearly interpolated between the two heights.

2.5.2. Roughness lengths. The aerodynamic surface roughness length of momentum (z_o) is simply prescribed in the model. Four different surface types are defined (water, tundra, ice and snow, see Table 1) and z_o is specified for each of these. On the ice sheet $\ln(z_o)$ is interpolated as a linear function of height going from the ice isotherm at level h_{ice} with a value of $z_o = 20$ mm to the snow isotherm at level h_{snow} of $z_o = 1$ mm. The larger roughness length for ice reflects the increased 'bumpiness' of ice surfaces, where hummocks of around 2–3 m are observed near the ice margin.

The aerodynamic surface roughness length for water is derived from the equations given by Garratt (1977) for smooth and rough surfaces as

$$\begin{aligned} z_o &= 0.11\frac{\nu}{u_*} \qquad \text{for} \qquad u_* < \left(\frac{0.11g}{\alpha_c}\nu\right)^{1/3} \\ z_o &= \frac{\alpha_c}{g}u_*^2 \qquad \text{for} \qquad u_* > \left(\frac{0.11g}{\alpha_c}\nu\right)^{1/3} \end{aligned} \quad (23)$$

where ν is the viscosity of air, g the acceleration due to gravity, u_* the friction velocity and Charnocks constant is $\alpha_c = 0.016$.

The scalar surface roughness lengths for temperature (z_h) and water vapour (z_q) on ice and snow surfaces are specified using the formulation from Andreas (1987), which is based on surface renewal theory. In this formulation the temperature roughness length is expressed as a function of roughness Reynolds number, $Re_* = u_* z_o/\nu$, where ν is the viscosity of air. z_h is determined from:

$$\ln\left(\frac{z_h}{z_o}\right) = 0.317 - 0.565\ln(Re_*) - 0.183\ln(Re_*)^2 . \tag{24}$$

Andreas also gives a separate formulation for the water vapour roughness length, but this differs only slightly from that of temperature, and so these two roughness lengths are assumed to be equivalent in the simulations.

The above formulation is slightly modified in the model according to Smeets (2000), who suggests that the most appropriate length scale for momentum in Eq. (24) is determined by the micro-scale crystal structure and not by the large-scale ice hummocks. This would appear to be a more appropriate length scale for the molecular diffusion processes associated with surface renewal theory. As such, a constant $z_{\text{oflat}} = 1$ mm is used to calculate z_h on both ice and snow, representing the micro-scale structure of the surface, throughout the model.

The scalar roughness lengths for tundra surfaces are determined from the relationship

$$\ln\left(\frac{z_{h,q}}{z_o}\right) = -2 \tag{25}$$

and above water by

$$\ln\left(\frac{z_{h,q}}{z_o}\right) = 2.5Re_*^{1/4} - 2. \tag{26}$$

Both these relationships are taken from Garratt (1992). The above roughness lengths, when dependent on u_* or Re_*, are updated in the model at every time step.

2.5.3. Subsurface model. The subsurface model is a simple 15-layer temperature diffusion model where englacial and deep soil processes such as absorption of shortwave radiation, refreezing and soil moisture content variations are ignored. Density, thermal diffusivity and heat capacity are taken as constant with depth and are specified according to the four surface types given in Table 1. Ice and snow subsurface parameters are specified in a similar fashion to the surface roughness lengths. That is, a linear function of height bounded at the maximum height h_{snow} by the snow parameters and at the minimum height h_{ice} by the ice parameters.

The deepest layer in the subsurface model is 10 m for all surface types, and the temperature at this level is held constant according to the yearly average value calculated with Eq. (22). The shallowest level is set at a depth of 5 mm and the grid points are logarithmically stretched inbetween. The top boundary condition is the net surface energy flux as calculated from the surface energy budget, Eq. (31). The numerical scheme uses a fully implicit time step to solve the diffusion equation. The equation solved is

$$\frac{\partial T_{ss}}{\partial t} = \frac{\partial}{\partial z_s}\left(\kappa_s \frac{\partial T_{ss}}{\partial z_s}\right) \tag{27}$$

where the subscript ss stands for subsurface and the thermal conductivity $k_s = \kappa_s \rho_s c_s$, where κ_s is the thermal diffusivity, ρ_s the density and c_s the specific heat.

The surface specific humidity of ice, snow and water is set to the saturated value based on surface temperature and the Clausius–Clapeyron equation. For tundra surfaces, a surface relative humidity of 50% is assumed.

Initialisation of the subsurface temperature with depth is based on the analytical solution to the temperature diffusion equation using the sinusoidal varying temperatures from Eq. (22) as the upper boundary condition.

2.5.4. Albedo. Of all the surface parameters only albedo is allowed to vary during the course of the simulation and is not coupled to Eq. (22). This is done using a two-layer snow model where the upper snow layer has an initial depth of zero and the lower snow layer an initial depth equal to 2/3 of the annual precipitation, taken from Ohmura and Reeh (1991). The top layer is a fresh snow layer where snow is deposited once every 6 d for 6 h at a rate commensurate with the mean annual precipitation rate. The snow albedo is determined as a function of melt for both layers as follows:

$$\alpha_{\text{snow}} = \alpha_{\text{firn}} + (\alpha_{\text{f snow}} - \alpha_{\text{firn}})\exp\left(\frac{-M}{M^*}\right) \tag{28}$$

with the maximum value of fresh snow $\alpha_{\text{f snow}} = 0.85$, and of firn $\alpha_{\text{firn}} = 0.6$. M is the accumulated melt and M^* is a characteristic melt scale with a value of 600 mm w.e. This value is based on a comparison with observed albedo change at sites S5 and S6 on the K-transect, see Section 3. The above equation describes the effect of metamorphosis in the snow pack and the associated change in albedo and follows the same form as that proposed by Ranzi and Rossi (1991). Both snow layers are allowed to melt, the lower layer melting only once the top layer has disappeared.

As the depth of a snow layer decreases the transition from the overlaying layer with albedo α_1 and depth d_1 to the underlying ice or snow layer α_2 is described by the following equation:

$$\alpha = \alpha_1 + (\alpha_2 - \alpha_1)\exp\left(\frac{-d_1}{d^*}\right) \tag{29}$$

which describes the patchiness of the snow cover (Oerlemans and Knap, 1998) and is parameterised so that surface albedo α varies exponentially with the depth of the snow layer d_1. The characteristic snow depth d^* used in this model is 1.6 cm.

The background albedo, α_{bg}, is prescribed using a similar parameterisation to Zuo and Oerlemans (1996), which allows the ice albedo to increase towards and above the equilibrium line in the following way:

$$\alpha_{\mathrm{bg}} = \frac{(\alpha_{\min} + \alpha_{\max})}{2} + \frac{(\alpha_{\max} - \alpha_{\min})}{\pi} \times \arctan\left[c_{\mathrm{bg}}\left(\frac{h}{ELA} - 1\right)\right] \tag{30}$$

where $\alpha_{\min} = 0.5$, $\alpha_{\max} = \alpha_{\mathrm{firn}}$, $c_{\mathrm{bg}} = 10$, h is the elevation and ELA is the long-term equilibrium line altitude taken from Reeh (1991) and parameterised as a function of latitude. The ELA in this parameterisation is held fixed during the simulation.

2.6. *The surface energy balance model*

The surface energy flux is calculated directly from the model according to

$$\mathrm{GFL} = \mathrm{NSW} + \mathrm{NLW} + \mathrm{HFL} + \mathrm{EFL} \tag{31}$$

and is defined as positive downwards. Each term is described below.

$\mathrm{NSW} = S_{\mathrm{s}}(1 - \alpha)$: The net shortwave radiation where S_{s} is the surface global radiation calculated from Eq. (19).

$\mathrm{NLW} = L\downarrow_{\mathrm{s}} - L\uparrow_{\mathrm{s}}$: The net longwave radiation at the surface where both the upward and downward longwave radiation fluxes are calculated using the emissivity scheme described in Section 2.3.

$\mathrm{HFL} = -\rho_{\mathrm{a}} c_p \overline{w\theta}_{\mathrm{s}}$: The sensible heat flux calculated from the turbulent vertical temperature flux where ρ_{a} is the density of air and $c_p = 1006$ J kg^{-1} K^{-1}.

$\mathrm{EFL} = -\rho_{\mathrm{a}} L_{\mathrm{e}} \overline{wq}_{\mathrm{s}}$: The latent heat flux calculated from the turbulent vertical water vapour flux where $L_{\mathrm{e}} = 2.5 \times 10^6$ J kg^{-1} is the latent heat of vaporisation of water.

GFL: The total net energy flux which is used as the upper boundary condition for the subsurface model, Section 2.5.3.

2.7. *Forcing parameters*

The synoptic wind field, $U_{\mathrm{g}}(x, y)$ and $V_{\mathrm{g}}(x, y)$, is prescribed from ECMWF analysis data, which are available with a horizontal resolution of roughly 70 km. The 700 hPa geo-potential pressure level is used to determine the synoptic pressure gradient, and from this geostrophic winds. This pressure level has an approximate elevation of 3000 m a.s.l., and as such intersects the surface where the ice sheet rises above this elevation. Though errors are expected when the ECMWF pressure level is extrapolated below the surface in this region, the 700 hPa level has been chosen because it is representative of the geostrophic flow above the ABL in the ablation zone, the region of most interest in this study. The synoptic pressure field is assumed to be barotropic, and so geostrophic winds are constant with height. It is updated every 12 h and linearly interpolated between these periods. The velocity field at the top of the model is set to the geostrophic values.

The synoptic, or ambient, temperature field $\Theta_{\mathrm{o}}(x, y, z)$ is also specified using ECMWF analysis data. As with the synoptic wind fields, Θ_{o} is updated and linearly interpolated every 12 h. The Θ_{o} field is determined by linearly fitting the vertical temperature profiles from the analysis data at levels 27–19, which corresponds to elevations of 900–4000 m a.s.l., respectively, when the surface elevation is at sea level. In this way a surface reference value $\Theta_{\mathrm{o\,ref}}(x, y)$ and a lapse rate $\gamma_{\mathrm{o\,ref}}(x, y)$ is determined for each grid point.

Specific humidity is similarly specified from ECMWF analysis data using the average relative humidity field from levels 27–23. Specific humidity is determined by taking the relative humidity field to be constant with height. Relative humidity is updated during the simulation at the top and lateral boundaries only.

The total cloud cover is taken from ECMWF analysis data and inserted at a constant height of approximately 3500 m a.s.l.. Cloud cover is used for the attenuation of shortwave radiation, Eq. (21), and for the longwave radiation scheme, Section 2.3. The liquid water content of the clouds is calculated from Albrecht et al. (1990), and the cloud depth is taken to be 500 m in order to determine the liquid water emissivity $\varepsilon_{\mathrm{lw}}$ at cloud height. $\varepsilon_{\mathrm{lw}}$, calculated in this fashion, is very close to unity, and so the insertion of clouds is effectively the same as the placement of a black body at the height of the cloud base.

Surface temperatures are specified using the monthly mean ECMWF analyses skin temperature in all areas not associated with the Greenland topography. These monthly means are linearly interpolated and updated during the simulation.

2.8. *Topography*

The Greenland topography and land/ice/sea mask is taken from the EKHOLM 0.02° data set (Ekholm, 1996). This data set is converted to an equidistant 5 km grid using a general stereographic projection centered at 72° N, 42° W. When using model resolutions larger than 5 km, grid points are simply stepped over: no interpolation of data points is employed. Smoothing of the data is carried out over the rough tundra region.

Topographical features not associated with Greenland are not represented in the model. This means that Ellesmere Island, to the north-west of Greenland, is not represented topographically. However, the monthly mean surface temperature of this region is retained in the sea surface temperatures.

2.9. *Numerics*

The model grid is a terrain-influenced vertically stretched grid, extending from the surface up to an elevation of 5000 m a.s.l.. The lowest grid level at sea level is 2 m but decreases slightly with elevation to 1.5 m on top of the ice sheet. In this study 20 vertical levels are used and the horizontal grid spacing is 20 km. The model domain extends a minimum of 200 km over sea on all sides of the Greenland land mass.

The computational grid used in the model is an equidistant grid ($\tilde{x}, \tilde{y}, \tilde{z}$). In order to determine the transformation metrics necessary for converting to the actual spatial coordinates (Section 2.1) this grid is first stretched logarithmically in the vertical, with the lowest grid level at 2 m, and then transformed to a terrain-influenced coordinate system. The transformation metrics J_{zz}, J_{zx} and J_{zy} are numerically determined from the transformed grid itself. The various prognostic and diagnostic fields are defined on a staggered grid of the Arakawa-C type.

The lateral boundaries are all above sea. Wind and perturbation temperature fields are solved at the boundaries as two-dimensional (2-D) solutions, along the boundaries, to the top boundary conditions. Specific humidity is determined at the top and side boundaries using the synoptic temperature profile, Θ_{o}, and the ECMWF relative humidity field. The top boundary conditions are fixed perturbation temperature ($\Theta = 0$), humidity and wind, which are set to their ECMWF analysis values as defined in Section 2.7.

The numeric scheme is a simple forward-in-time scheme where the turbulent diffusion equation is implicitly solved and advection is treated with a first-order upwind scheme. A time step of 6 min is used, and the longwave radiation is calculated every fifth time step.

The simulated fields for wind, perturbation temperature and specific humidity are relaxed into their ECMWF values at the top of the model domain using a relaxation scheme in the following form:

$$\frac{\partial \Phi}{\partial t} = -C_{\mathrm{r}}(z)\frac{\Phi - \Phi_{\mathrm{o}}}{\tau_{\mathrm{r}}} \tag{32}$$

where Φ is the parameter being relaxed, Φ_{o} the ambient field it is relaxed to and τ_{r} is the relaxation time, which has a value of 4 h. $C_{\mathrm{r}}(z)$ is a height-dependent function that increases from 0 at the surface to 1 at the top of the model domain and is specified by

$$C_{\mathrm{r}}(z) = \frac{1}{2} + \frac{1}{2}\sin\left[\frac{\pi}{2}\left(2\frac{z}{z_{\mathrm{d}}} - 1\right)\right] \tag{33}$$

where z is the model height above the surface and z_{d} is the depth of the model domain. At a height of 500 m, roughly the height of the ABL, $C_{\mathrm{r}}(z)$ would take on a value of approximately 0.01, giving an effective relaxation time of 400 h.

Advection of the ambient temperature field Θ_{o}, radiative divergence and the partial time derivative of Θ_{o}, Eq. (11), are assumed to be accounted for in the ECMWF model above the ABL. These terms are only calculated at grid points within the ABL itself, the height of the ABL being defined as the level at which the turbulent kinetic energy goes to zero.

3. Comparison with observations

The model is run using ECMWF input fields taken from the 1998 ECMWF analysis data starting on 20 May 1998, day 140, and ending on 28 August 1998, day 240. Hourly and daily means of model variables are saved for several positions on the ice sheet and tundra during the run. These correspond to positions of known observations and six of these sites, positioned on the ice sheet and shown in Fig. 1, are used for a direct comparison with the model simulation.

Results from the model are shown as daily means of wind speed and temperature for a number of observational sites and also in terms of the summer seasonal averages. This is taken as the 90 d period starting on day 150 and finishing at the end of the model run, day 240, which allows a 10 d spin up period at the beginning of the simulation.

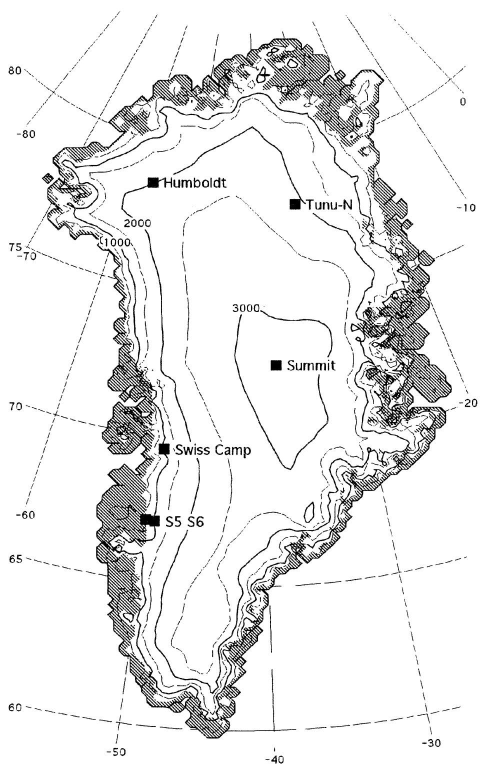

Fig. 1. Positions of the six AWS sites used in the comparison. Elevation is shown in metres with contours separated by 500 m. The tundra is shown as the shaded region.

3.1. General characteristics

The simulated summer average 2 m temperature field for the Greenland ice sheet is shown in Fig. 2a. Summer mean temperatures in the accumulation zone of the ice sheet reach $-11\ ^\circ$C, whilst the maximum average temperature near the ice margin is around $5\ ^\circ$C. The average 2 m temperature lapse rate over the entire ice sheet is -5.1 K km^{-1}, ranging from -7.8 K km^{-1} in the accumulation zone to -2.6 K km^{-1} in melt regions. The average ECMWF-derived free atmospheric lapse rate over the entire ice sheet is -5.0 K km^{-1}.

In Fig. 2b the simulated summer average 2 m wind field and ECMWF 700 hPa pressure level height are also shown. A high-pressure region can be seen above Greenland as the result of atmospheric cooling above the ice sheet. This high-pressure synoptic field introduces a general anticyclonic circulation which enhances the downslope katabatic forcing. Wind speeds can be seen to increase towards the ice margin, and this is chiefly the result of increased katabatic forcing. However, wind speeds are also retarded by the prescribed surface roughness length, which increases towards the ice edge.

3.2. Comparison with observed meteorological variables

A number of meteorological stations are available for a comparative study with the 1998 GABLM simulation. Six of these stations positioned on the ice sheet, Table 2 and Fig. 1, are selected for verification. Unfortunately only three of these stations are situated in the ablation zone, S5 and S6 from the Utrecht University K-transect and Swiss Camp, now part of the PARCA network. The stations Humboldt, Tunu-N and Summit from the PARCA network in the accumulation zone are also used (Steffen et al., 1996).

A comparison is made of 2 m daily average values for temperature and wind speed, which are the two most important meteorological components that define turbulent fluxes. The results are shown in Figs. 3 and 4 as a function of time. Included in the comparison are ECMWF analysis data of the same 2 m variables. Interpolated data can be obtained from ECMWF down to a resolution of 0.5° in both latitude and longitude. This means that interpolated data obtained near the ice margin may be a combination of both tundra and ice sheet points.

For the three ablation zone sites the boundary layer model reproduces quite well the observed daily

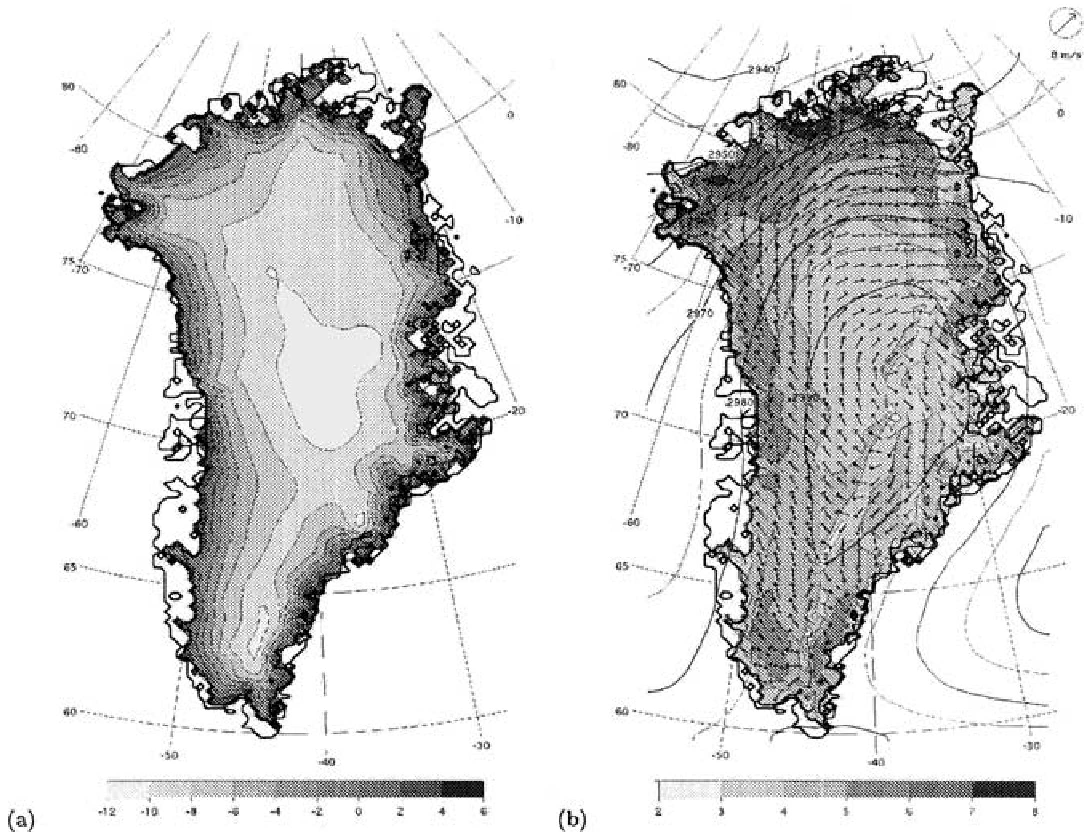

Fig. 2. (a) Simulated average summer 2 m temperatures in °C. (b) Simulated average summer 2 m wind and synoptic pressure fields over the Greenland ice sheet. The shading indicates the magnitude of the wind vector in m s^{-1} and the contours indicate the height, in metres, of the 700 hPa pressure level taken from ECMWF analysis data. Arrows showing wind vectors are placed at every third grid point.

average temperatures, as does the ECMWF analysis for Swiss Camp. In contrast, ECMWF analysis temperatures are far too high at site S6, on average 3.2 °C. S6 is located a similar distance from the ice edge as Swiss Camp, approximately 35 km, but in this case the interpolated data obtained from ECMWF consists of both ice sheet and tundra values. The nearest available ECMWF data point for S5 is situated on the tundra and so has not been used in the comparison.

Temperatures at the three accumulation sites are also reasonably well simulated during the summer period with the GABLM, although all sites are slightly

Table 2. *Positions and elevations of the observational sites used in the comparison*

Site	Latitude	Longitude	Elevation (m)	Model elevation (m)	Model slope (°)
S5	N 67°05′56″	W 50°06′25″	484	456	1.00
S6	N 67°04′35″	W 49°22′44″	1021	958	1.01
Swiss Camp	N 69°34′06″	W 49°18′57″	1149	1126	0.91
Humboldt	N 78°31′36″	W 56°49′50″	1995	1988	0.21
Tunu-N	N 78°01′00″	W 33°59′38″	2113	2096	0.21
Summit	N 72°34′47″	W 38°30′16″	3254	3242	0.07

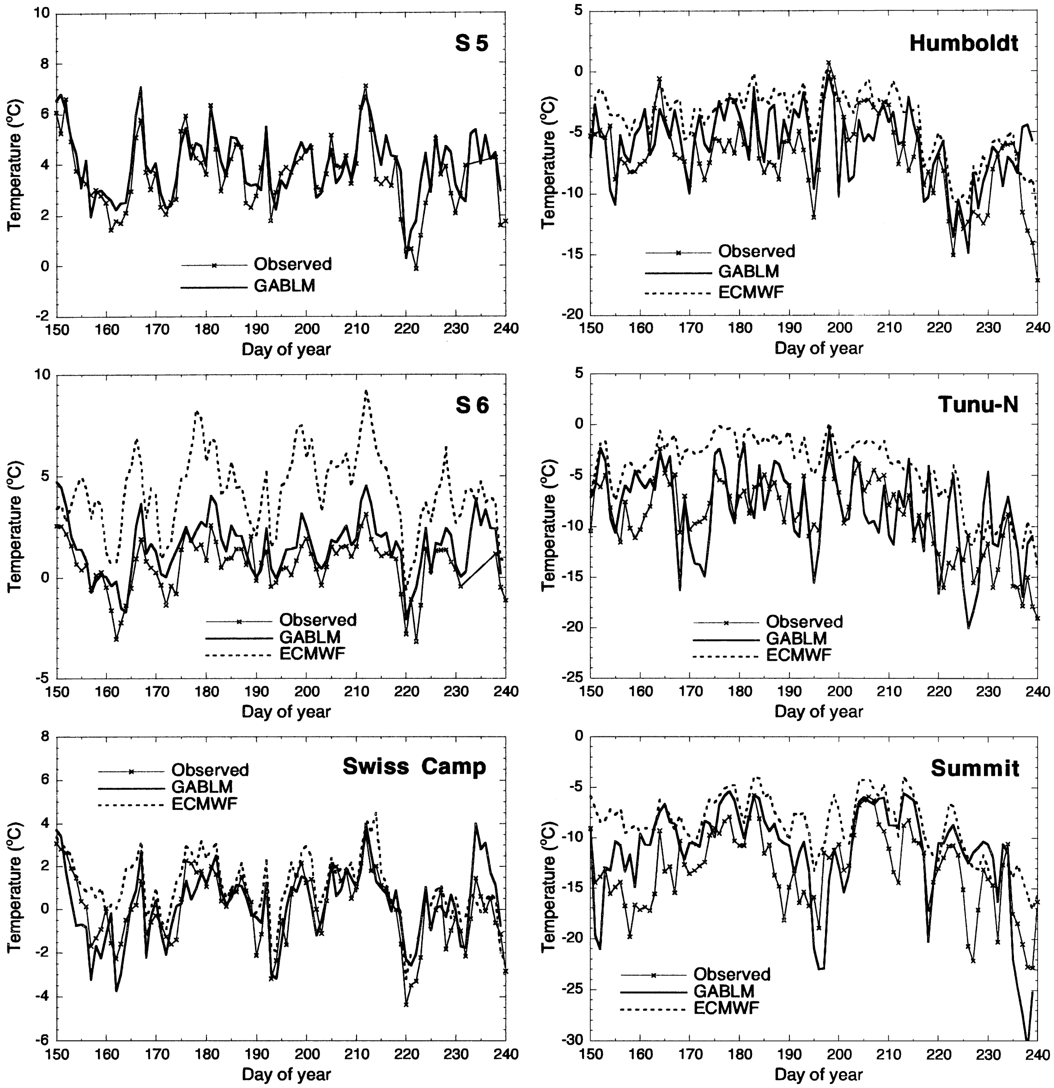

Fig. 3. Observed, simulated (GABLM) and ECMWF analysis data for 2 m temperature from day 150 to 240. The positions of the six sites shown are listed in Table 2.

too warm, the mean temperature difference being from 0.5 to 1.6 °C. ECMWF analysis data also tend to be too warm at all these sites, by up to 4.4 °C, which is most likely due to the lower snow albedo value of 0.7 used in the ECMWF model.

In Fig. 4 the observed and simulated wind speeds are shown. The GABLM is capable of reproducing wind speeds in the ablation zone quite well. In this region katabatic forcing plays an important role in the determination of wind speed and direction. The lower-resolution ECMWF model cannot accurately simulate this effect, and so ECMWF wind speeds will be too low in the ablation zone. The higher resolution of the GABLM allows wind speeds to be more accurately determined, but at site S5, which is within 7 km of the ice edge, GABLM simulated wind speeds are still too low. With a horizontal resolution of 20 km the model determined slope at site S5 is 1° compared with 2° derived from the 5 km resolution terrain model. This difference in slope directly affects the katabatic

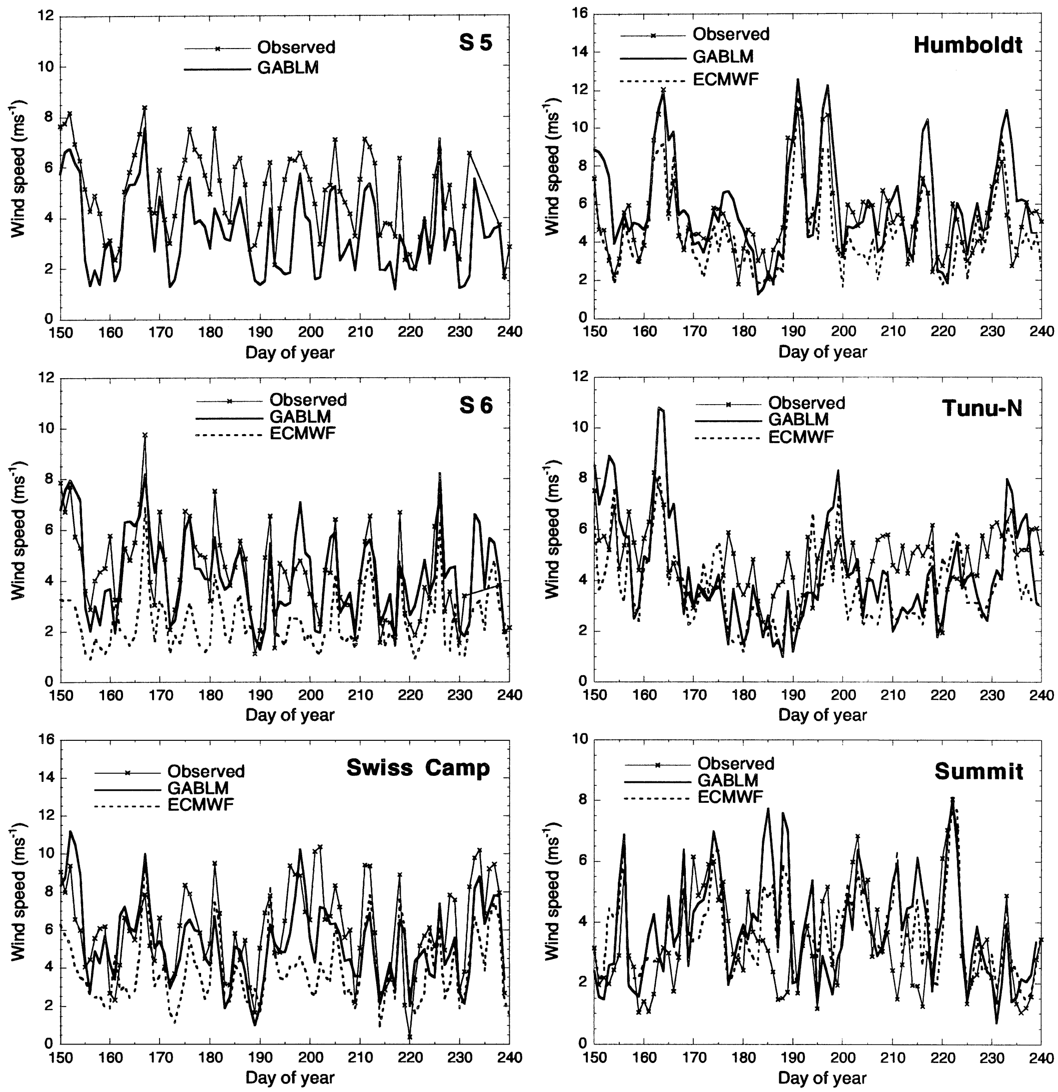

Fig. 4. Observed, simulated (GABLM) and ECMWF analysis data for 2 m wind speed from day 150 to 240. The positions of the six sites shown are listed in Table 2.

forcing and hence wind speeds; see e.g. Denby (1999). Investigations with the model using a 10 km horizontal resolution grid over a limited area show that the simulated wind speed is substantially improved at this site with increased resolution. For the accumulation sites the average GABLM wind speeds are within 1 m s^{-1} of the observed values and improve slightly on the ECMWF estimates.

In Table 3 the mean values of observed temperature, specific humidity, wind speed, net shortwave and net longwave radiation for this period are listed for each of the AWS sites. Also included is the mean difference between the simulated and observed values, along with the difference between ECMWF derived and observed values. At most sites NSW radiation is overestimated, particularly at Swiss Camp, where the mean difference is 29 W m^{-2}. This has a two-fold cause. Firstly, the observed albedo at Swiss Camp is higher than the simulated albedo, and secondly the parameterisation for shortwave radiation cloud transmission, Section 2.4,

Table 3. *Mean observed values for temperature, specific humidity, wind speed, net shortwave radiation (NSW) and net longwave radiation (NLW) for the the 90 d summer period shown in Figs. 3 and 4*[a].

SITE	Temperature (°C)			Specific humidity (g kg^{-1})			Wind speed (m s^{-1})			NSW (W m^{-2})		NLW (W m^{-2})	
S5	3.6	(+0.4)					4.9	(−1.5)		117	(−6.0)	−32	(+10)
S6	0.6	(+0.8)	*(+3.2)*				4.3	(0.0)	*(−2.0)*	122	(−8.0)	−56	(+20)
Swiss Camp	0.2	(+0.1)	*(+0.8)*	3.1	(+0.1)	*(+0.2)*	6.0	(−0.6)	*(−2.8)*	69	(+29)	−54	(+4.0)
Humboldt	−6.9	(+0.8)	*(+2.8)*	2.8	(+0.1)	*(+0.5)*	5.3	(+0.7)	*(−0.8)*	33	(+18)	−46	(−1.0)
Tunu-N	−9.0	(+0.5)	*(+4.4)*	2.3	(+0.3)	*(+0.6)*	4.7	(−0.4)	*(−1.7)*	32	(+21)	−49	(−7.0)
Summit	−13.1	(+1.6)	*(+4.1)*	2.0	(+0.4)	*(+0.6)*	3.3	(+0.5)	*(+0.2)*	31	(+24)	−42	(+7.0)

[a]The mean difference between 2 m GABLM and observed values is shown in parentheses, and the mean difference between the 2 m ECMWF analysis for temperature, specific humidity and wind speed is shown in italics and parentheses. Humidity measurements are not available at sites S5 and S6.

appears to underestimate the influence of clouds. This last discrepancy is common to all sites with the exception of S5, which is the lowest site.

The NLW radiation is also overestimated at the majority of sites. Possible explanations for this discrepancy come from incorrect cloud cover, incorrect cloud height, or inaccuracies in the emissivity scheme itself. Cloud cover in the Summit region is also quite high, with a mean value of 0.8 for the summer period. This may also help to explain the higher simulated temperatures found in this region.

Since GABLM is driven by simplified ECMWF analysis data and ECMWF model resolution is sufficiently good to resolve processes on the ice sheet away from the margins, it is not expected that the GABLM will improve the simulations in this region. However, daily average temperatures on the ice sheet are in general better represented after downscaling with the GABLM. This is most likely due to differences in surface parameters, such as albedo, but it does indicate that such a downscaling model can be used to improve near surface variables such as temperature even when surface parameters are not correctly represented in the forcing model.

3.3. *Surface energy balance*

Even though direct measurements of the turbulent flux components of the SEB were not made at the observational sites, it is instructive to look at the simulated SEB components. These are shown for the six observational sites, in order of elevation, in Fig. 5. At site S5, closest to the ice sheet margin and at the lowest elevation, the SEB is dominated by the absorption of solar radiation (NSW); however, the sensible heat flux (HFL) makes up 42% of the net surface energy flux (GFL). As elevation increases the sensible and latent heat fluxes decrease. At Swiss Camp the latent

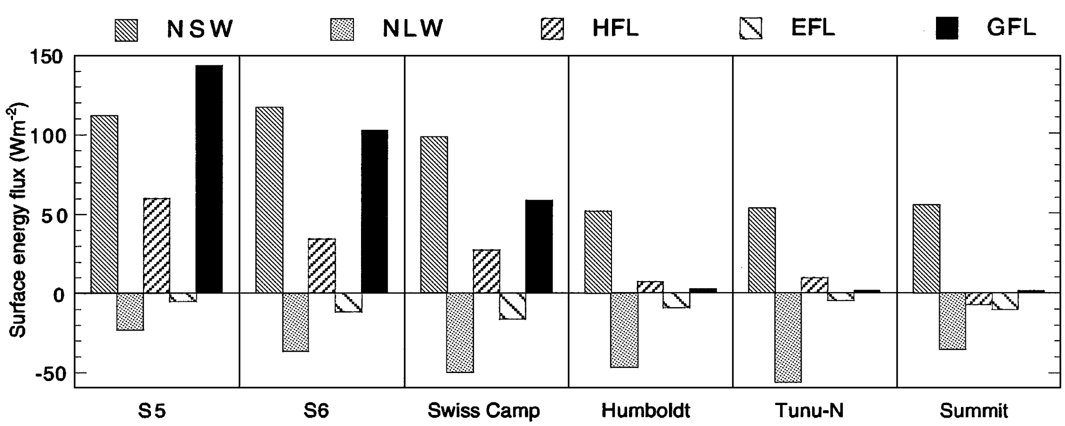

Fig. 5. Mean summer surface energy budget for the six observational sites. NSW is the net shortwave radiation, NLW the net longwave radiation, HFL the sensible heat flux, EFL the latent heat flux and GFL the total heat flux, all in W m^{-2}.

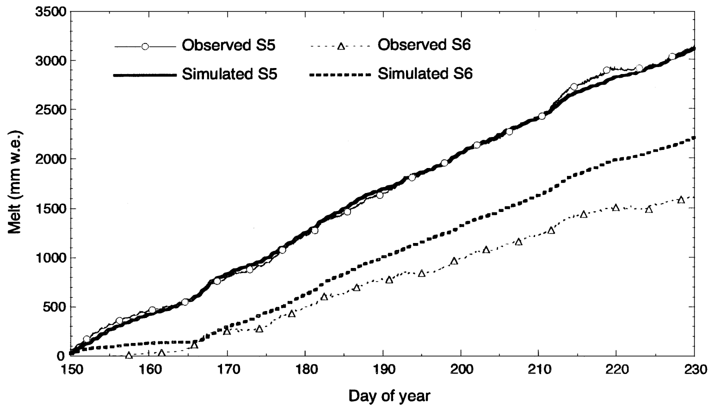

Fig. 6. Comparison of GABLM simulated melt and observed melt at sites S5 and S6. The density of ice, $\rho = 910$ kg m^{-3}, is used to calculate the observed melt in mm w.e.

heat flux (EFL) is of similar magnitude to HFL but of opposite sign.

In the accumulation zone, where little or no melt occurs, the SEB is dominated by the radiation balance and turbulent heat fluxes tend to balance the energy budget so that GFL is very small in this region. At Summit, HFL is found to be small but negative, indicating that a convective ABL, as opposed to the stable ABL normally found on the ice sheet, is dominant. The presence of a convective ABL at high elevations has been observed by Box (2001) using AWS from the PARCA network. At Summit, observations show the ABL to be unstable for 20% of the entire year, occurring exclusively during summer when shortwave radiation is at a maximum.

3.4. Melt

The resulting melt from the simulation can be compared to measurements made at S5 and S6, Fig. 6, where sonic ranging height meters were present up to day 230, when the AWS were retrieved for maintenance. At S5 the observed melt during this period is 3125 mm w.e. and the simulated melt is 3105 mm w.e. At S6 the observed melt is 1612 mm w.e. and the simulated melt is 2204 mm w.e.

The discrepancy between the simulated and observed values at S6 can be partially accounted for by the radiation budget. On average the simulated net radiation budget at S6 is 12 W m^{-2} too high. If this were to be converted entirely to melt then this would account for 350 mm w.e. of the excess melt, leaving a difference of 200 mm w.e. The higher temperatures at this site, when compared to observations, will also lead to an overestimate of the turbulent flux component. It should be noted that for at least some of the melt season snow is present at S6 so the "observed" water equivalent melt is an upper limit.

At S5 the comparison is particularly good. At this site the GABLM radiation budget is only 4 W m^{-2} too low. However, it was noted in Section 3.2 that the simulated wind speeds at this site were also too low due to the poorly resolved surface slope, and so one would expect an underestimate of the turbulent heat fluxes at this site. This is to some degree compensated for by the slightly higher simulated temperature.

At site S5, where melt is well simulated, the surface is made up of hummocky ice, well drained and with little winter snow cover. This is opposed to site S6, which is locally flatter, with poorer drainage, and snow covered for some of the ablation season. Refreezing of melt water at this site could account for a significant portion of the local mass balance.

4. Discussion and conclusion

Simulations of the Greenland ABL described in this paper make use of simplified global model data output, in this case taken from ECMWF analysis data, and downscales these data using a dynamic atmospheric boundary layer model, GABLM. By doing this, resolution can be enhanced and the ABL can be modelled with improved results in an 'off line' fashion.

The results achieved by the GABLM simulations improve significantly on direct results from the ECMWF analysis data for the 1998 summer period investigated. The near surface meteorological variables of temperature, wind speed and specific humidity are all improved upon for the sites investigated. In general, 2 m wind speeds are well simulated except near the ice sheet margin, e.g. site S5, where the 20 km model resolution underestimates surface slope and hence katabatic forcing.

Two-metre temperatures tend to be too high at almost all sites. This may indicate that the model does not correctly simulate the temperature inversion of the ABL or that surface parameters, such as albedo, or processes within the snow pack need to be improved upon. The largest discrepancy in the ablation zone is found at site S6, where the 2 m temperature is found to be 0.8 °C higher than that observed. This discrepancy cannot be blamed entirely on the overestimated net radiation budget of 12 W m^{-2} since the surface was found to be melting for 71% of the simulated period and during this time the surface temperature would be unaffected by energy balance considerations. However, upwind temperatures may also be too high, and these would have been advected downslope to this site. At accumulation sites, where melt does not occur, the surface temperature is directly affected by the surplus radiation budget simulated with the GABLM. This is chiefly due to the poorness of the parameterisation of the shortwave radiation transmission used in the model. This scheme, based on measurements along the K-transect during GIMEX (van de Wal, 1994, and Konzelmann et al., 1994), overestimates the incoming shortwave radiation by up to 50 W m^{-2} during both clear sky and cloudy periods. The parameterisation works reasonably well at the accumulation sites, which are close to the region for which it was initially developed.

It is also important to note that any large-scale errors in wind and temperature fields that occur in the ECMWF analysis data will automatically be carried over to the GABLM. Thus the simulations are directly dependent on the quality of the ECMWF analysis. This is perhaps mirrored in the unrealistically high cloud covers produced by ECMWF in the Summit region of the ice sheet.

The simulated melt is found to correspond well to observations made at site S5 in the ablation zone, and to be too large (35%) at a higher ablation site, S6. The discrepancy at S6 is partly accounted for by the difference in observed and simulated radiation fluxes but is also a result of the simplified subsurface model used. Refreezing of melt water is not included in the subsurface model. Indeed, the total simulated melt is clearly an upper limit on the total ablation, since a significant proportion of melt will be refrozen in the snow pack. Any future estimates of ablation using this or similar models will require a better representation of the subsurface processes.

Despite this, GABLM has been shown to be a useful tool in determining the ABL and the SEB of the Greenland ice sheet. The potential of this method is that GCM or weather prediction model output can be used off line to generate improved estimates of the surface energy balance, essential for determining the total mass balance of the Greenland ice sheet.

5. Acknowledgements

We thank Jason Box of the University of Colorado for the PARCA AWS data used in this comparison. We also thank all those at the Institute for Marine and Atmospheric Research, Utrecht University who are concerned with the development and maintenance of the two AWS sites used in this study. Thanks are also due to the reviewers, whose insightful comments have helped to improve this article. This research was chiefly funded by the Dutch National Research Programme on Global Air Pollution and Climate Change (NOP II project 013 001236.10).

Appendix: Turbulence closure scheme

The two prognostic equations used to describe the model turbulence are E, turbulent kinetic energy, and $\overline{ww}$ the vertical momentum variance.

$$\frac{\mathrm{d}E}{\mathrm{d}t} = MP_E + BP_E - \epsilon + J_{zz}\frac{\partial}{\partial\tilde{z}}\left(c_s\frac{E}{\epsilon}\overline{ww}J_{zz}\frac{\partial E}{\partial\tilde{z}}\right) \tag{A1}$$

$$\begin{aligned}\frac{\mathrm{d}\overline{ww}}{\mathrm{d}t} = {} & \frac{2}{3}c_2(1-2c_2'F)MP_E \\ & +2\left(1-\frac{2}{3}c_3\right)BP_E - \frac{2}{3}(1-c_1)\epsilon \\ & -\frac{\overline{ww}}{E}(c_1+2c_1'F)\epsilon \\ & +J_{zz}\frac{\partial}{\partial\tilde{z}}\left(3c_s\frac{E}{\epsilon}\overline{ww}J_{zz}\frac{\partial\overline{ww}}{\partial\tilde{z}}\right)\end{aligned} \tag{A2}$$

where

$$MP_E = -J_{zz}\left(\overline{uw}\frac{\partial U}{\partial\tilde{z}} + \overline{vw}\frac{\partial V}{\partial\tilde{z}}\right) \tag{A3}$$

Table 4. *Closure constants used in this paper [taken from Denby (1999)]*

c_1	c_2	c_3	c'_1	c'_2	d_1	d_2	d_3	d'_1	c_ϵ	d_ϵ	c_s	C_B	κ
1.82	0.6	0.3	0.98	0.05	3.01	0.78	0.33	3.8	0.76	0.77	0.2	1.69	0.4

$$BP_E = \frac{g}{\Theta_o}\overline{w\theta} \tag{A4}$$

$$\epsilon = c_\epsilon \frac{E^{3/2}}{l} \tag{A5}$$

$$\frac{1}{l^2} = \frac{1}{(\kappa z)^2} + \frac{1}{l_a^2} \tag{A6}$$

$$F = \frac{l}{\kappa z} \tag{A7}$$

The asymptotic length scale l_a is equal to the buoyant length scale l_b under stable conditions as follows

$$l_b = \kappa C_B \left(\frac{\overline{w^2}}{N^2}\right)^{1/2} \tag{A8}$$

where N is the Brunt–Väisälä frequency and C_B is a constant. Under unstable conditions it is given by the boundary layer length scale proposed by Mellor and Yamada (1974):

$$l_a = 0.2\frac{\int_0^{z_d} zE\,dz}{\int_0^{z_d} E\,dz} \tag{A9}$$

where z_d is the height of the model domain.

Using these equations and the second-order closure scheme derived in Denby (1999) the vertical turbulent diffusion coefficients K_Φ, which relate vertical fluxes to their mean gradients via

$$K_\Phi = -\overline{w\Phi}\left(\frac{\partial\Phi}{\partial z}\right)^{-1} \tag{A10}$$

are calculated in the following way

$$K_{m,h,q} = C_{m,h,q}\frac{E^{1/2}l}{c_\epsilon}. \tag{A11}$$

The coefficients $C_{m,h,q}$ are dependent on stability and are given as follows:

$$C_m = \frac{A_7\overline{ww}/E - A_8(1-d_2)/d_1 N_R C_h}{1 + A_8/d_1 N_R} \tag{A12}$$

$$C_h = \frac{\overline{ww}/E}{d_1 + d'_1 F + A_9 N_R} \tag{A13}$$

$$C_q = \frac{\overline{ww}/E - 0.5A_9 N_R C_h}{d_1 + d'_1 F + 0.5A_9 N_R} \tag{A14}$$

where

$$N_R = \frac{g}{\Theta_o}\frac{l^2}{Ec_\epsilon^2}\frac{\partial\overline{\Theta}}{\partial z} \tag{A15}$$

$$A_7 = \frac{1 - c_2 + 1.5c_2c'_2F}{c_1 + 1.5c'_1F} \tag{A16}$$

$$A_8 = \frac{1 - c_3}{c_1 + 1.5c'_1F} \tag{A17}$$

$$A_9 = \frac{1 - d_3}{d_\epsilon} \tag{A18}$$

The constants used in the above equations are listed in Table 4. For a complete description and derivation of the equations mentioned in this section see Denby (1999).

REFERENCES

Albrecht, B. A., Fairall, C. W., Thomson, D. W. and White, A. B. 1990. Surface-based remote sensing of the observed and the adiabatic liquid water content of stratocumulus clouds. *Geophys. Res. Lett.* **17**, 89–92.

Anderson, D. A., Tannehill, J. C. and Pletcher, R. H. 1984. *Computational fluid mechanics and heat transfer*. Hemisphere Publishing, 252.

Andreas, E. L. 1987. A theory for the scalar roughness and the scalar transfer coefficients over snow and sea ice. *Boundary-Layer Meteorol.* **38**, 159–184.

Box, J. E. 2001. *Surface water vapour exchanges on the Greenland ice sheet derived from automatic weather station data*. Ph.D. thesis, University of Colorado, USA.

Denby, B. 1999. Second-order modelling of turbulence in katabatic flows. *Boundary-Layer Meteorol.* **92**, 67–100.

Denby, B., Greuell, W. and Oerlemans, J. 2002. Simulating the Greenland atmospheric boundary layer. Part II: Energy balance and climate sensitivity. *Tellus* **54-A**, this issue.

Ekholm, S. 1996. A full coverage, high-resolution, topographic model of Greenland computed from a variety of digital elevation data. *J. Geophys. Res.* **21**, 21961–21972.

Gal-Chen, T. and Somerville, R. C. J. 1975. On the use of coordinate transformation for the solution of the Navier–Stokes equations. *J. Comput. Phys.* **17**, 209–228.

Garratt, J. R. 1977. Review of drag coefficients over oceans and continents. *Mon. Wea. Rev.* **105**, 915–929.

Garratt, J. R. 1992. *The atmospheric boundary layer*. Cambridge University Press, Cambridge, UK.

Garratt, J. R. and Brost, R. A. 1982. Radiative cooling effects within and above the nocturnal boundary layer. *J. Atmos. Sci.* **38**, 2730–2746.

Greuell, W. and Konzelmann, T. 1994. Numerical modelling of the energy balance and the englacial temperature of the Greenland ice sheet. Calculations for the ETH camp location (West Greenland, 1155 m a.s.l.). *Global Planet. Change* **9**, 79–90.

Hanjalić, K. and Launder, B. E. 1972. A Reynolds stress model of turbulence and its application to thin shear flows. *J. Fluid. Mech.* **52**, 609–638.

Iqbal, M. 1983. *An introduction to solar radiation*. Academic Press, Toronto, Canada.

Konzelmann, T., van de Wal, R. S. W., Greuell, W., Bintanja, R., Henneken, E. A. C. and Abe-Ouchi, A. 1994. Parameterization of global and longwave incoming radiation for the Greenland ice sheet. *Global Planet. Change* **9**, 143–164.

Mellor, G. L. and Yamada, T. 1974. A hierarchy of turbulence closure models for planetary boundary layers. *J. Atmos. Sci.* **31**, 1791–1806.

Oerlemans, J. and Knap, W. H. 1998. A 1 year record of global radiation and albedo in the ablation zone of the Morteratschgletscher, Switzerland. *J. Geophys. Res.* **44**, 231–238.

Ohmura, A. 1987. New temperature distribution maps for Greenland. *Z. Gletscherkd. Glazialgeol.* **23**, 1–45.

Ohmura, A. and Reeh, N. 1991. New precipitation and accumulation maps for Greenland. *J. Glaciol.* **37**, 140–148.

Pielke, R. A. 1984. *Mesoscale meteorological modelling*. Academic Press, Orlando, FL, USA.

Ranzi, R. and Rossi, R. 1991. Physically based approach to modelling distributed snow melt. In: *IAHS Publication 205*, 141–152.

Reeh, N. 1991. Parameterization of melt rate and surface temperature on the Greenland ice sheet. *Polarforschung*, **59**, 113–128.

Reeh, N., Mayer, C., Miller, H., Thomsen, H. H. and Weidick, A. 1999. Present and past climate control on fjord glaciations in Greenland: Implications for IRD-deposition in the sea. *Geophys. Res. Lett.* **26**, 1039–1042.

Rodgers, C. D. 1967. The use of emissivity in atmospheric radiation calculations. *Quart. J. R. Meteorol. Soc.* **73**, 67–92.

Shir, C. C. 1973. A preliminary numerical study of atmospheric turbulent flows in the idealized planetary boundary layer. *J. Atmos. Sci.* **30**, 1327–1339.

Smeets, C. J. P. P. 2000. *Stable boundary layer over a melting glacier: turbulence characteristics and surface energy balance*. Ph.D. thesis, Free University of Amsterdam, The Netherlands.

Steffen, K., Box, J. E. and Abdalati, W. 1996. Greenland climate network: GC-Net. In: *CRREL 96-27 Special report on glaciers, ice sheets and volcanoes, trib. to M. Meier* (ed. S. C. Colbeck) 101–123.

van de Wal, R. S. W. 1994. An energy balance model for the Greenland ice sheet. *Global Planet. Change* **9**, 115–131.

Welch, R. and Zdunkowski, W. 1976. A radiation model of the polluted atmospheric boundary layer. *J. Atmos. Sci.* **33**, 2170–2184.

Zuo, Z. and Oerlemans, J. 1996. Modelling albedo and specific balance of the Greenland ice sheet: calculations for the Søndre Strømfjord transect. *J. Glaciol.* **42**, 305–317.